Progressive evolution of the viscous dissipation mechanism from the macroscale to the nanoscale

Yi-Feng Wang[1,2], **Zhi-Hui Cai**[1,2], **Yi-Bo Wang**[1,2], **Shu-Rong Gao**[1,2],
Yan-Ru Yang[1,2], **Shao-Fei Zheng**[1,2,†], **Duu-Jong Lee**[3,4,†] and
Xiao-Dong Wang[1,2,†]

[1]State Key Laboratory of Alternate Electrical Power System with Renewable Energy Sources,
North China Electric Power University, Beijing 102206, PR China

[2]Research Center of Engineering Thermophysics, North China Electric Power University, Beijing 102206,
PR China

[3]Department of Mechanical Engineering, City University of Hong Kong, Kowloon Tong 999077,
Hong Kong

[4]Department of Chemical Engineering & Materials Science, Yuan Ze University, Chung-Li 32003, Taiwan

Recent studies of viscous dissipation mechanisms in impacting droplets have revealed distinct behaviours between the macroscale and nanoscale. However, the transition of these mechanisms from the macroscale to the nanoscale remains unexplored due to limited research at the microscale. This work addresses the gap using the many-body dissipative particle dynamics (MDPD) method. While the MDPD method omits specific atomic details, it retains crucial mesoscopic effects, making it suitable for investigating the impact dynamics at the microscale. Through the analysis of velocity contours within impacting droplets, the research identifies three primary contributors to viscous dissipation during spreading: boundary-layer viscous dissipation from shear flow; rim geometric head loss; and bulk viscous dissipation caused by droplet deformation. This prompts a re-evaluation of viscous dissipation mechanisms at both the macroscale and nanoscale. It reveals that the same three kinds of dissipation are present across all scales, differing only in their relative intensities at each scale. A model of the maximum spreading factor (β_{max}) incorporating all forms of viscous dissipation without adjustable parameters is developed to substantiate this insight. This model is validated against three distinct datasets representing the macroscale, microscale and nanoscale, encompassing a broad spectrum of Weber numbers, Ohnesorge numbers and contact angles. The satisfactory agreement between the model predictions and the data signifies a breakthrough in establishing a universal β_{max} model applicable across all scales. This model demonstrates the consistent

† Email addresses for correspondence: shaofeizheng56@gmail.com, tuclee@cityu.edu.hk,
wangxd99@gmail.com

nature of viscous dissipation mechanisms across different scales and underscores the importance of integrating microscale behaviours to understand macroscale and nanoscale phenomena.

Key words: drops and bubbles

---

1. Introduction

A droplet impacting a solid surface is a familiar occurrence in everyday life, offering a wide range of complex outcomes such as spreading, retraction, deposition, splashing, bouncing and breakup (Josserand & Thoroddsen 2016). Despite its commonplace nature, the study of droplet impact dynamics on solid surfaces remains a vibrant area of research. Since being initially documented by Worthington (1876), this field has continued to thrive in recent years. Substantial efforts have been made to unravel the secret of impact dynamics, encompassing diverse approaches such as experimental studies (Bertola 2009; Visser *et al.* 2012, 2015; Lee *et al.* 2016*a*; Yang *et al.* 2018; Srivastava & Kondaraju 2020), numerical simulations (Eggers *et al.* 2010; Kobayashi *et al.* 2016; Lee *et al.* 2016*a*; Koishi, Yasuoka & Zeng 2017; Bordbar *et al.* 2018; Du *et al.* 2021*a*) and theoretical analyses (Ukiwe & Kwok 2005; Attané, Girard & Morin 2007; Laan *et al.* 2014; Lee *et al.* 2016*b*; Wang *et al.* 2019, 2020*a*,*b*).

The vitality of studying droplet impact on solid surfaces stems from the various parameters governing this seemingly simple phenomenon. This includes a balance of competing forces and the influence of various surface characteristics. In the case of droplet impact, inertial, capillary and viscous forces are the primary influencers if the droplet diameter (D_0) is less than the capillary length (2.7 mm for water, for example). The key dimensionless numbers to quantify this interplay are the Weber number ($We = \rho D_0 V_0^2/\gamma$), representing the ratio of inertial to capillary forces; the Reynolds number ($Re = \rho D_0 V_0/\mu$), indicating the ratio of inertial to viscous forces; and the Ohnesorge number ($Oh = We^{1/2}/Re = \mu/(\rho D_0 \gamma)^{1/2}$), denoting the ratio of viscous to inertial-capillary forces. Surface features also play a crucial role, encompassing intrinsic wettability, roughness, microstructure and topography. The intrinsic wettability, in particular, is effectively quantified by the intrinsic contact angle, θ, which is the angle at the three-phase contact line of an equilibrium sessile droplet on a smooth surface. These diverse parameters mean that even the most straightforward scenario of a droplet impacting a smooth surface is governed by a complex group of dimensionless numbers, including We, Oh (Re) and θ. This richness of parameters endows the impact dynamics with fascinating mechanisms, continually inspiring in-depth studies and research in this area.

One of the critical areas of interest in droplet dynamics research is investigating the energy conversion mechanism of impacting droplets. This is often analysed by modelling the maximum spreading factor ($\beta_{max} = D_{max}/D_0$), which is a ratio of the maximum spreading diameter (D_{max}) to its original diameter (D_0). This modelling is frequently based on the energy conservation equation, which tracks the droplet's journey from its initial state to the maximum spreading state, as adopted and refined in various studies (Yarin & Weiss 1995; Clanet *et al.* 2004; Laan *et al.* 2014; Lee *et al.* 2016*b*; Wildeman *et al.* 2016). The energy conservation equation can be expressed as

$$E_{k,0} + E_{s,0} = E_{s,max} + E_{dis}, \tag{1.1}$$

where subscripts of k, s and *dis* represent the kinetic energy, surface energy and viscous dissipation; *0* and *max* stand for the initial state and the maximum spreading state,

respectively. The initial spherical shape of droplets leads to simple expressions for initial kinetic and surface energy ($E_{k,0}$ and $E_{s,0}$). The assumption of a cylindrical shape at the maximum spreading state, supported by most studies (Pasandideh-Fard *et al.* 1996; Ukiwe & Kwok 2005; Du *et al.* 2021*a*), allows for the derivation of $E_{s,max}$. However, as compared with the surface energy, which depends only on shape, the viscous dissipation during spreading is also highly influenced by velocity gradients within impacting droplets, presenting a significant challenge in its quantification. Historically, assumptions about velocity gradients have evolved. Initially, there were assumptions of violent velocity gradients throughout droplets, considering only the $\partial V_z/\partial z$ (Chandra & Avedisian 1991) or $\partial V_r/\partial z$ (Madejski 1976) components, where V_z and V_r represent the velocities in the impact and spreading directions, respectively, and z stands for the coordinate in the impact direction. Recent studies, however, have recognised that the velocity gradient $\partial V_r/\partial z$ in the thin boundary layer near solid walls predominantly contributes to viscous dissipation during spreading (Mao, Kuhn & Tran 1997; Ukiwe & Kwok 2005; Attané *et al.* 2007; Visser *et al.* 2015; Srivastava & Kondaraju 2020; Du *et al.* 2021*a*). To estimate this dissipation, models for the thickness of the boundary layer (δ) have been proposed, such as $\delta = 2D_0 Re^{-1/2}$, derived by analogising the plane stagnation flow with the flow inside impacting droplets (Pasandideh-Fard *et al.* 1996; Ukiwe & Kwok 2005). In a comparison by Ukiwe & Kwok (2005) of theoretical β_{max} models based on the boundary-layer viscous dissipation assumption with experimental results on weak hydrophilic and hydrophobic surfaces, the models (Pasandideh-Fard *et al.* 1996; Ukiwe & Kwok 2005) tend to overpredict the maximum spreading factor in a moderate range of Weber numbers (approximately from 30 to 100). Beyond this range, however, there is a better alignment between the theoretical predictions and experimental observations.

Contrary to previous assumptions, the groundbreaking study by Wildeman *et al.* (2016) numerically analysed the impact of a droplet on free-slip solid surfaces. This analysis specifically aimed to exclude the boundary-layer viscous dissipation. Interestingly, the results revealed that significant dissipation of the initial kinetic energy still occurred during spreading, suggesting the presence of an alternative form of viscous dissipation. This dissipation was identified not as boundary-layer viscous dissipation but rather as a geometric head loss at the entrance of spreading rims, where a rapid reduction in velocity leads to the dissipation of nearly half of the initial kinetic energy. Crucially, this rim head loss was also observed in impacts on no-slip surfaces, where it similarly dissipated approximately half of the initial kinetic energy (Wildeman *et al.* 2016). This finding is further supported by the distribution of viscous dissipation observed by Lee *et al.* (2016*a*).

These insights imply that viscous dissipation in millimetre-sized droplets impacting solid surfaces results from both the boundary layer and rim. This understanding may explain why models that only consider boundary-layer viscous dissipation tend to overestimate β_{max} in a moderate range of Weber numbers on weakly hydrophilic and hydrophobic surfaces (Pasandideh-Fard *et al.* 1996; Ukiwe & Kwok 2005). After incorporating this additional mechanism of viscous dissipation, the β_{max} model proposed by Wildeman *et al.* (2016) achieves a more accurate fit for a broad range of Weber numbers, from 30 to 3000, on surfaces with contact angles ranging from 90° to 180°.

Recently, there has been a surge in interest in the nanoscale impact dynamics on solid surfaces, principally due to the emergence of nanodroplet-based technologies such as nanoscale ink-jet printing (Galliker *et al.* 2012) and the preparation of high-entropy materials (Glasscott *et al.* 2019). Observing nanodroplet impact processes through direct experimentation is challenging due to the limitations of high-speed cameras. Consequently, molecular dynamics (MD) simulations, serving as 'virtual experiments' have become the primary investigative tool. Through MD simulations, several studies

(Li, Zhang & Chen 2015; Wang *et al.* 2019, 2020*a*,*b* 2021*a*,*b*, 2022*a*,*b*, 2023; Xie *et al.* 2020) have identified that nanodroplets exhibit distinct dynamics compared with millimetre-sized droplets, highlighting significant scale effects. One notable scale effect is the presence of velocity gradients throughout the entire nanodroplet (Li *et al.* 2015), as opposed to only in specific regions. This discovery implies that models developed for macroscale droplets fail to predict β_{max} at the nanoscale, which is subsequently proven by Li *et al.* (2015). In response, recent studies have reevaluated the estimation of viscous dissipation during spreading, accounting for velocity gradients across the entire droplet at the nanoscale. Various velocity distributions have been proposed to establish β_{max} models (Li *et al.* 2015; Wang *et al.* 2019, 2020*a*,*b*, 2022*b*). For example, Wang *et al.* (2020*a*) suggested $V_r = V_s rz/(RH)$ and $V_z = -z^2 V_s/(RH)$, where R is the spreading radius, H is the droplet height, r is the coordinate in the spreading direction and V_s is the spreading velocity. Despite differing assumptions among nanoscale studies, there is a consensus that viscous dissipation at this scale occurs throughout the entire droplet. However, the mechanism underlying these scale effects remains unclear. No studies have directly explored why the similarity in velocity gradients breaks down when transitioning from macroscale to nanoscale droplets. It is generally believed that due to their minimal diameters, nanodroplets are entirely within the boundary layer (Li, Li & Chen 2017; Wang *et al.* 2020*a*).

In droplet impact dynamics, the dominant forms of viscous dissipation vary significantly between the macroscale and nanoscale: at the macroscale, boundary-layer and rim viscous dissipation predominantly influence the dynamics, while at the nanoscale, viscous dissipation throughout the entire droplet becomes the critical factor, referring to as scale effects by recent studies. Nonetheless, it is essential to consider that the internal flow characteristics of droplets should seamlessly transition from the macroscale to the nanoscale. Within this context, the major obstacle to understanding scale effects is the lack of research on impacting droplets at the microscale. Achieving this comprehensive understanding of droplet impact dynamics across all scales presents significant challenges. Experimental studies to date have found it challenging to investigate the impact dynamics of droplets with diameters smaller than 40 µm approximately, primarily due to the limitations of high-speed camera technology (Visser *et al.* 2012, 2015). On the computational front, the typical diameter of droplets studied in current MD simulations is of the order of 10 nm. This limitation is primarily due to computational performance constraints, as highlighted in studies by Li *et al.* (2015, 2017), Wang *et al.* (2019, 2020*a*,*b*, 2021*a*,*b*, 2022*a*,*b*, 2023), Xie *et al.* (2020) and Du *et al.* (2020). Therefore, a noticeable research gap exists for droplet diameters approximately between 10 nm and 40 µm. This range, referred to as the microscale in this study, remains a largely unexplored territory.

The recent development of the many-body dissipation particle dynamics (MDPD) method offers a promising avenue for advancing our understanding of droplet impact dynamics at the microscale. This innovative coarse-grained numerical method strategically omits specific atomic-level details while retaining crucial mesoscopic effects. Such an approach allows for studying larger-scale systems than those typically examined in MD simulations. This capability of MDPD has been supported by the studies of Warren (2001, 2003), Nie, Zhong & Fang (2019), Chen, Nie & Fang (2020) and Zhao *et al.* (2021). Given its advantage, the MDPD method is expected to be particularly effective for investigating the impact dynamics of droplets within the microscale range. This fills the critical gap in current research methodologies, bridging the divide between nanoscale-focused MD simulations and the limitations of high-speed camera technology in capturing macroscale phenomena. The application of MDPD thus holds significant

potential for providing new insights into droplet dynamics at this vital but previously inaccessible scale.

The primary goal of this research is to decipher the mechanisms of viscous dissipation during spreading across all scales. This work first addresses the research gap at the microscale using MDPD simulations. Through these simulations, the velocity distribution within impacting droplets is meticulously extracted and analysed, gaining insights into the viscous dissipation mechanisms at the microscale. This analysis is pivotal in revealing that the progressive flow characteristics shift from the macroscale to the microscale and eventually to the nanoscale. Tracing this transition reveals how viscous dissipation mechanisms evolve from the macroscale to the nanoscale. As a result of this comprehensive study, a full-scale β_{max} model is developed and validated. This model is supported by extensive data covering the macroscale, microscale and nanoscale, verifying the viscous dissipation mechanism throughout the full scales.

2. Simulation method

The MDPD method is a coarse-grained approach wherein each coarse particle symbolises a cluster of real atoms/molecules. This method ignores atomic details while maintaining mesoscopic effects (Zhao *et al.* 2021). Consequently, MDPD simulations are particularly adept at exploring microscale dynamics. All simulations are implemented using the LAMMPS (large-scale atomic/molecular massively parallel simulator) software package. Each simulation includes three steps: the creation of initial systems; the establishment of interactions between particles; and the implementation of simulation procedures.

As figure 1 shows, the initial step features a water droplet (the map between the MDPD liquid and water to be discussed later) and a solid substrate. The droplet is positioned at a distance of 5 DPD units (the units will be elucidated later) from the solid substrate to avoid premature contact, where the DPD stands for dissipation particle dynamics. Moreover, the system is filled with gas particles to replicate a nitrogen environment of 100 kPa, similar to an atmospheric environment. The simulation's dimensions are $80 \times 80 \times 48$, with periodic boundary conditions applied along the *x*- and *y*-axes and a fixed boundary condition on the *z*-axis. The droplet and solid substrate are initially generated using simple cubic crystal structures.

In MDPD simulations, water–water (*w-w*), solid–solid (*s-s*) and water–solid (*w-s*) particle interactions are governed by three distinct forces, as proposed by Groot & Warren (1997) and Warren (2001, 2003). These forces are the conservative force (F_{ij}^C), the dissipative force (F_{ij}^D) and the random force (F_{ij}^R), i.e.

$$F_{ij} = F_{ij}^C + F_{ij}^D + F_{ij}^R, \tag{2.1}$$

where F_{ij} represents the force exerted by particle *j* on particle *i*. The mathematical expressions for these forces are formulated as

$$F_{ij}^C = A\omega_c(r_{ij})e_{ij} + B(\rho_i + \rho_j)\omega_d(r_{ij})e_{ij}, \tag{2.2}$$

$$F_{ij}^D = -\gamma_d \omega_D(r_{ij})(e_{ij}v_{ij})e_{ij}, \tag{2.3}$$

$$F_{ij}^R = \sigma \omega_R(r_{ij})\xi_{ij}\Delta t^{-1/2}e_{ij}. \tag{2.4}$$

The relative position and velocity vectors, denoted as e_{ij} and v_{ij}, are determined by r_{ij}/r_{ij} and $v_i - v_j$, respectively. In (2.2), the conservative force comprises two components: the attractive and repulsive forces, modulated by parameters *A* and *B*. The weight functions,
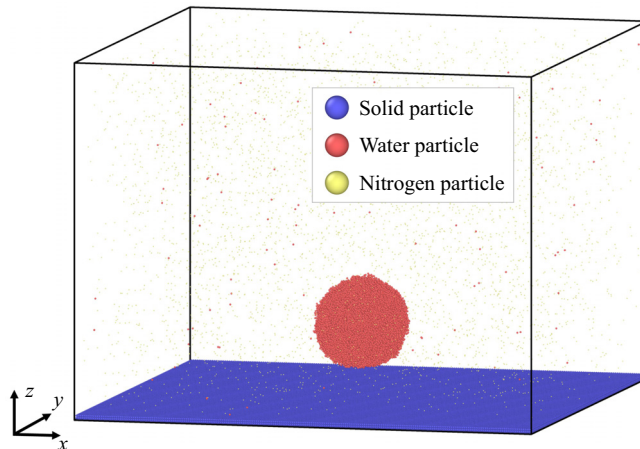
Figure 1. The schematic of the simulation system containing a droplet above a solid substrate after achieving equilibrium. The system is filled with nitrogen particles to replicate a nitrogen environment of 100 kPa, similar to an atmospheric environment.

ω_c (for the attractive force) and ω_d (for the repulsive force), are computed using the expressions $1 - r_{ij}/r_c$ and $1 - r_{ij}/r_d$, respectively, where r_c and r_d signify the cutoff distances for these forces. For accurately simulating the liquid–vapour interface, the soft repulsion is tailored to depend on local density. The local density ρ_i is calculated using the formula $\rho_i = \sum_{i \neq j} \omega_\rho(r_{ij})$, where ω_ρ is defined as $15(1 - r_{ij}/r_d)^2/2\pi r_d^3$ with a cutoff distance of r_d. According to the fluctuation–dissipation theorem, the dissipative and random force function is akin to a pairwise Brownian dashpot, and the coefficients can be expressed as $\sigma^2 = 2\gamma_d k_B T$, where k_B represents the Boltzmann constant, T is the temperature of the system, γ_d and σ are the coefficients for dissipative and random forces, respectively. When γ_d is given, σ can be calculated by the expression. In (2.3) and (2.4), the weight functions ω_D and ω_R, which are dependent on the distance r, are computed by $\omega_D(r_{ij}) = \omega_R(r_{ij})^2 = (1 - r_{ij}/r_c)^2$. The variable ξ_{ij} is a Gaussian random number with zero mean and unit variance, and Δt denotes the time step used in the simulations.

The MDPD method, with its local-density-dependent soft repulsion, has been proven to successfully create a stable liquid–vapour interface (Ghoufi, Malfreyt & Tildesley 2016). Additionally, the dynamics of bulk liquids have been validated through the Navier–Stokes (NS) equations (Arienti et al. 2011), bolstering confidence in the MDPD method's ability to simulate droplet behaviour accurately. Beyond the droplet, the interaction between solid and liquid is also critical. The MDPD method's soft potential is recognised as the reason for enabling the simulation of a more extensive system compared with MD simulations (Murtola et al. 2009); however, this approach can lead to a challenge: when the density of solid is low, non-physical penetration by the liquid may occur. A high-density solid is employed in the present simulations to avoid non-physical penetration of liquid. Recent studies also proposed various methods to prevent non-physical penetration, such as modifying the solid–liquid potentials (Li et al. 2018) and employing artificial bounce-back schemes (Li et al. 2013). Nevertheless, these treatments tend to create a no-slip surface condition, contradicting the observed slip effect at small scales (Arienti et al. 2011). Hence, this study does not apply these methods.

The final challenge is establishing a correlation between MDPD-simulated liquids and their experimental counterparts. The MDPD method, being a coarse-grained approach,

Parameter	Symbol	Value
Attractive coefficient	$A_{w\text{-}w}$	−40
Repulsive coefficient	$B_{w\text{-}w} = B_{w\text{-}s}$	8
System temperature	$k_B T$	1
Dissipation parameter	γ_d	24
Cutoff radius	r_c	1
Repulsive interaction range	r_d	0.89
Time step	Δt	0.01

Table 1. The parameters of MDPD simulations.

does not focus on specific liquids but on general interactions, as represented in (2.2)–(2.4). Consequently, while MDPD simulations accurately represent the general dynamics of liquids (Yamada, Yuan & Sunden 2015), this generality poses difficulties in directly mapping an MDPD-simulated liquid to an experimental liquid. Fortunately, a significant advancement was made by Jamali *et al*. (2015), who introduced a generalised equation of state for MDPD liquids. This equation enables the calculation of dimensionless compressibility, effectively bridging the gap between a simulated MDPD liquid and an experimental one. Based on this work, the simulation parameters are carefully chosen and set, as shown in table 1, to ensure that the dimensionless compressibility of the MDPD-simulated liquid aligns with that of water. The values of γ_d, r_c and r_d do not alter for different pairs of interactions in our simulations. Because the solid particles are fixed to their positions, the parameters of A_{s-s} and B_{s-s} are not included in this table. The interactions of nitrogen particles (*n-n*) and between nitrogen and other particles (*n-w* and *n-s*) are described in see supplementary material and table S1 available at https://doi.org/10.1017/jfm.2024.911. According to our tests, the density ratio of vapour to liquid in MDPD simulations is approximately 2.9×10^{-5} when phase equilibrium between liquid and vapour is achieved. This density ratio closely matches the experimental value of 2.5×10^{-5} for water, indicating that the MDPD liquid can be mapped to water in experiments. Additionally, the density ratio of nitrogen gas to liquid in the MDPD simulation is 1.1×10^{-3}, aligning with that of a water droplet in a nitrogen environment at 100 kPa in experiments. Agreement on these properties facilitates a more accurate and meaningful comparison between simulations and experiments.

Once the MDPD-simulated liquid is mapped to an experimental one, the relationship between the actual physical units and the DPD units can be determined using the following formulae: $l^{real} = [L] \times l^{DPD}$ for length, $m^{real} = [M] \times m^{DPD}$ for mass and $t^{real} = [T] \times t^{DPD}$ for time. The quantities in square brackets indicate the scaling relationships between the actual and DPD units. Using the parameters in table 1, the density, surface tension and viscosity of the MDPD liquid are calculated as $\rho^{DPD} = 6.23$, $\gamma^{DPD} = 4$ and $\mu^{DPD} = 4.78$. In comparison, the properties of water at 300 K in experiments are as follows: $\rho = 996 \text{ kg m}^3$, $\gamma = 72 \text{ mN m}^{-1}$ and $\mu = 854 \text{ } \mu\text{Pa s}$. By aligning these physical properties, the scaling relationships are determined to be $[L] = 1.15 \times 10^{-8}$ m, $[M] = 2.43 \times 10^{-22}$ kg and $[T] = 1.16 \times 10^{-10}$ s. The diameter of droplets with a DPD diameter of 20 is 230 nm in the actual physical units.

The parameter A_{w-s} is not included in table 1 because it is an adjustable parameter to generate a range of surface wettability. For each value of A_{w-s}, a droplet is gently placed on the surface, allowing it to spread and then reach an equilibrium state spontaneously. Subsequently, the intrinsic contact angle at this A_{w-s} is determined by fitting the outer

$A_{w\text{-}s}$	-21	-25	-30	-32	-36	-37
$\theta/°$	164	147	137	125	109	100
$\cos\theta$	-0.96	-0.84	-0.73	-0.57	-0.33	-0.17

Table 2. Relationships between contact angles and the values of $A_{w\text{-}s}$.

contour of the droplet and measuring the angle at the three-phase contact line. Table 2 lists the contact angles used in this work and their corresponding values of A_{w-s}.

The implementation of simulation comprises two processes. The first is the equilibrium process, during which the centre of mass of the droplet is held fixed while the system undergoes relaxation over 200 000 time steps. Once the equilibrium process is completed, the simulation transitions into the impact process. In this process, the control of the droplet is released. Concurrently, the droplet is given with a velocity directed towards the substrate, leading to a variety of outcomes based on impact conditions.

The rarefaction and compressibility effects are discussed at the end of this section. Recent advancements in small-scale ink-jet printing technology have revealed that ink droplets can attain high impact velocities of the order of 100 m s^{-1} (Galliker *et al.* 2012). Similarly, this study also explores a broad velocity range from 25 to 600 m s^{-1}, creating a wide range of *We* spanning three orders of magnitude. This wide range suggests that the compressibility effect might be significant. The Mach number ($Ma = V_0/V_{sound}$, where V_{sound} represents the speed of sound) is often used to quantify the compressibility effect. Considering that our simulation system is filled with nitrogen like an atmospheric environment, V_{sound} is approximately equal to 340 m s^{-1}, so *Ma* ranges from 0.07 to 1.76. For $Ma > 1.2$, the droplet falls in a supersonic regime, indicating a possible strong compressibility effect. However, neither the experiments by Galliker *et al.* (2012) nor simulations from previous studies at the nanoscale (Li *et al.* 2017; Wang *et al.* 2021*b*) report significant compressibility effects. This occurrence can be attributable to the rarefaction effect that counteracts the compressibility effect. The Knudsen number ($Kn = L/D_0$, where L is the mean free path of gas molecules) signifies the strength of rarefaction effects. Based on the kinetic theory of gases, L is computed as $k_B T/(2^{1/2}\pi d^2 p)$ and is 64.5 nm, where the molecular diameter d is 0.38 nm for nitrogen and gas pressure p is 100 kPa. As a result, *Kn* is obtained as 0.28. This *Kn* value indicates that the gas environment is in the transitional flow regime, where rarefaction effects are pronounced (Gad-el-Hak 1999).

In the context of a moving solid particle within a gas environment, several studies (Zarin 1970; Loth 2008) have specifically examined the drag experienced by the particle across various gas environments and a broad spectrum of relative velocities between particles and gas environments. The particle Reynolds number, defined as $Re_p = \rho_g D_0 V_0/\mu_g = (\pi\gamma_h/2)^{1/2}Ma/Kn$, where γ_h is the specific heat ratio, ρ_g is the gas density and μ_g is the gas viscosity, is used to evaluate the relative strengths of compressibility and rarefaction effects. With the help of experimental data and direct simulation Monte Carlo method results, Zarin (1970) and Loth (2008) reported a nexus point of compressibility and rarefaction effects at a specific particle Reynolds number of $Re_p = 45$. At $Re_p = 45$, regardless of the values of *Ma* and *Kn*, the drag of a spherical particle remains constant. Furthermore, when $Re_p < 45$, *Ma* is relatively small compared with *Kn*, so the rarefaction effect is dominant, thereby supporting the incompressibility of the gas. This is confirmed by the agreement between the drag data for $Re_p < 45$ and the drag predicted by the

incompressible theories by Loth (2008). Therefore, $Re_p < 45$ can be a criterion indicating that compressibility effects will not take place and the gas still satisfies the incompressible assumption.

This criterion is applicable to droplet impacts because of the following reasons. The impact of droplets can be divided into two processes: the preimpact flight process and the impact process itself. In the preimpact flight process, droplets do not undergo significant deformation, remaining spherical throughout, which validates the applicability of the $Re_p < 45$ criterion for determining no compressibility effect. In the impact process, although strong deformation of the droplet occurs, suggesting that the criterion might not be directly applicable, the rapid deceleration reduces the velocity of droplets below the threshold that could induce compressibility effects. Based on this reason, if compressibility effects do not occur during the flight process, they would not take place in the entire impact process either. Thus, the $Re_p < 45$ criterion is considered effective for determining the absence of compressibility effects in droplet impacts and for confirming the incompressibility of the gas. The following aspect interprets the underlying mechanism of the rarefaction effect counteracting the compressibility effect (Loth *et al.* 2021). The compressibility effect tends to increase the pressure on the fore side of the particle, thereby increasing drag; however, the rarefaction effect can induce the velocity gradient on the surface, i.e. slip, therefore decreasing drag (Loth *et al.* 2021). Therefore, when the rarefaction effect is dominant, the possible compressibility effect can be effectively counteracted and make the gas still satisfy the incompressible assumption. In the nitrogen gas environment at 100 kPa, simulated in this work, with $\rho_g = 1.14$ kg m^{-3} and $\mu_g = 17.8$ µPa s, even at the maximum velocity $V_0 = 600$ m s^{-1} in our study, Re_p is only 8.9, considerably below the threshold of 45. Consequently, this confirms the dominance of the rarefaction effect and the gas is incompressible in our simulations.

3. Results and discussion

3.1. *Evidence of the existence of scale effects*

This section uses β_{max} as the key parameter to demonstrate the presence of scale-dependent viscous dissipation mechanisms. An established understanding is that spreading droplets on smooth surfaces is governed by dimensionless groups, including We, Oh and θ. According to this concept, if scale effects are absent and the values of all dominant dimensionless groups remain constant, β_{max} should be identical at all scales. Therefore, scale effects are tested by directly comparing β_{max} values at different scales while maintaining the same We, Oh and θ.

In MDPD simulations, the value of Oh is 0.21 for MDPD droplets with $D_0 = 20$ (DPD units). To maintain a consistent Oh of 0.21, the high-viscosity liquid (glycerol–water mixtures with 85 % glycerol concentration) at the macroscale and the extremely low-viscosity liquid (mW liquid, with a viscosity of just one-third that of water) at the nanoscale are chosen. Additionally, the surface wettability is also fixed at approximately 164°. Figure 2 shows the β_{max} versus We curves at different scales, with the macroscale data from the experimental study by Abolghasemibizaki *et al.* (2019) and the nanoscale data from this work using MD simulations (detailed method refer to Wang *et al.* (2022b)). As $We < 30$, the maximum spreading factors at different scales show negligible divergence. However, as We exceeds 30, deviation among the β_{max} values at different scales grows with increasing We, contradicting the traditional scale-independent behaviour. Consequently, this disparity confirms the presence of scale effects between different scales.
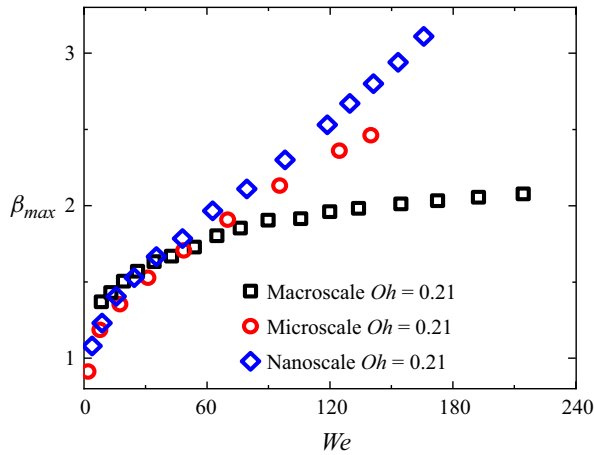
Figure 2. Comparison of β_{max} for impacting droplets at the macroscale (Abolghasemibizaki *et al.* 2019), the microscale and the nanoscale on superhydrophobic surfaces with $\theta = 163°$, $164°$ and $165°$, respectively.

3.2. *Understanding viscous dissipation mechanisms at different scales*

This section focuses on analysing the velocity contours of impacting droplets to decipher the viscous dissipation mechanism at the microscale. With an understanding at the microscale, the viscous dissipation mechanisms of the macroscale and the nanoscale could be revisited, and the whole picture of the viscous dissipation mechanism can be unveiled.

The velocity contours for an impacting droplet with a diameter of 230 nm on a surface with $\theta = 147°$ at $We = 235.6$ is shown in figure 3(*a–c*). The left-hand sides of the figures illustrate the contours of V_z, while the right-hand sides display those of V_r. The velocity profile near the solid wall at $r = 7.3$ in figure 3(*a*) is also highlighted in figure 3(*d*) to exhibit near-wall velocity gradients. A few observations are noticeable. First, the velocity gradients in the region highlighted by the blue square resemble those in the boundary layer seen in macroscale scenarios, i.e. $\mathrm{d}V_r/\mathrm{d}z$ is dominant. The difference is that the velocity at the liquid–solid interface is non-zero at the microscale against the validity of the no-slip boundary condition. This occurrence results in a weaker boundary-layer viscous dissipation than at the macroscale. Second, the spreading rims still occur during spreading, and V_r peaks at the entrance of spreading rims, as shown in the region marked by the green square in figure 3(*a–c*). When entering the rims, V_r rapidly decreases, offering a substantial gradient of $\mathrm{d}V_r/\mathrm{d}r$, indicative of rim geometric head loss. Third, within the bulk droplet, the velocity gradients are also violent but differ markedly from those in the boundary layer. Unlike $\mathrm{d}V_r/\mathrm{d}z$ observed in the boundary layer, $\mathrm{d}V_r/\mathrm{d}r$ and $\mathrm{d}V_z/\mathrm{d}z$ dominate the bulk droplet. Such a feature of velocity distribution is named extensional flow, whose viscous dissipation is mainly attributable to the deformation of droplets. Consequently, the viscous dissipation mechanism at the microscale is governed by three types of viscous dissipation: boundary-layer viscous dissipation due to shear flow near solid surfaces ($E_{dis,boundary}$); rim head loss at the entrance of spreading rims ($E_{dis,rim}$); and bulk viscous dissipation caused by extensional flow from droplet deformation ($E_{dis,bulk}$). This mechanism has also been further corroborated by additional observations from MDPD simulations in broad ranges of We and θ at the microscale.

Previous studies have examined the viscous dissipation mechanisms at both the macroscale and nanoscale. However, due to the distinct characteristics of velocity gradients at these scales, they have traditionally been considered opposites (Li *et al.* 2015; Wang
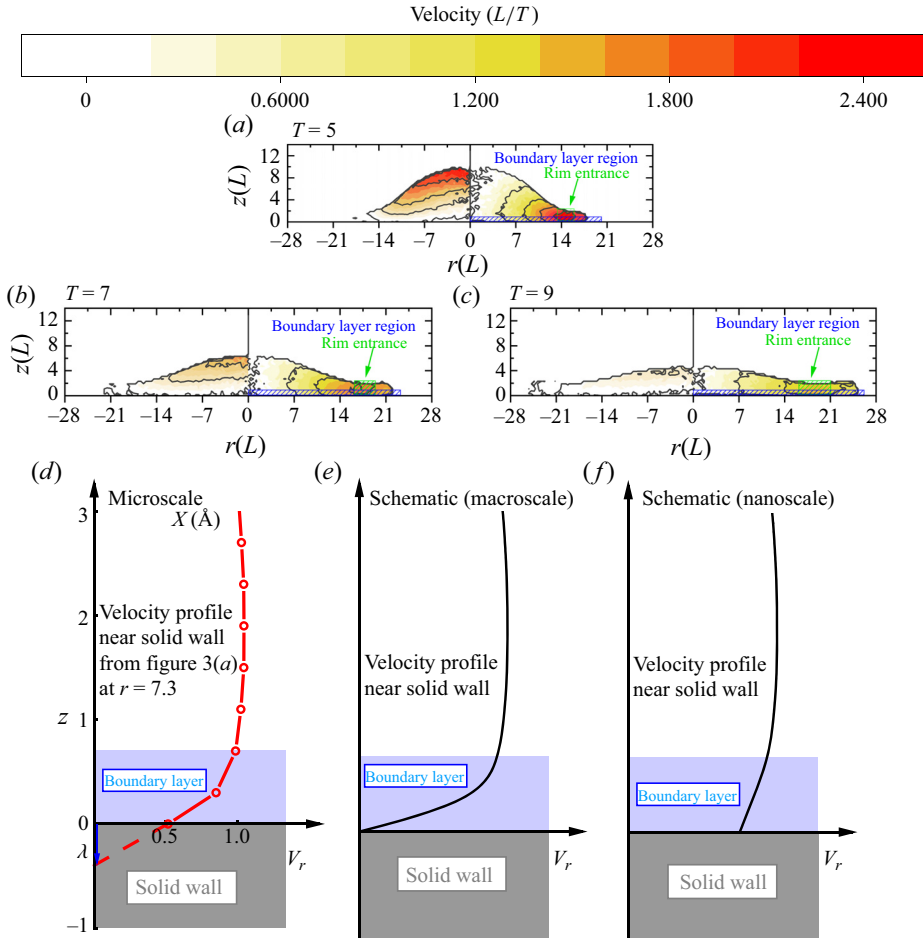
998 A21-10

Figure 3. (*a–c*) Velocity contours of microscale droplets impacting surfaces with $\theta = 147°$ at $We = 235.6$. (*d–f*) Velocity profiles near solid walls at the microscale, the macroscale and the nanoscale, respectively.

et al. 2020*a*). In this study, the viscous dissipation mechanism at the microscale has been uncovered, offering a valuable link that bridges the gap between the two extreme scales. This discovery presents a unique opportunity to explore how the viscous dissipation mechanism transitions from the macroscale to the nanoscale. To this end, the viscous dissipation mechanisms at the macroscale and the nanoscale are revisited below.

At the macroscale, only two types of dissipation, $E_{dis,boundary}$ and $E_{dis,rim}$, have been reported (Wildeman *et al.* 2016), while $E_{dis,bulk}$ is negligible, to our best knowledge. The no-slip condition is applicable to the boundary layer, as shown in figure 3(*e*). The model incorporating only $E_{dis,boundary}$ and $E_{dis,rim}$ accurately predicts β_{max} for low Oh droplets at the macroscale; however, the model would overestimate β_{max} for high Oh, with more pronounced overestimation on β_{max} with increasing Oh (Wildeman *et al.* 2016). This observation suggests that deformation-induced $E_{dis,bulk}$ is significant at high Oh. In fact, the droplet-deformation-induced dissipation commonly participates in the natural and industrial processes. For instance, the freely decaying oscillations of levitated droplets serve as evidence of this mechanism. In such processes, both $E_{dis,boundary}$ and $E_{dis,rim}$ are absent due to the lack of solid surfaces and rim formation, leaving only

deformation-induced $E_{dis,bulk}$ as the dominating dissipation mechanism. Furthermore, as *Oh* increases, the damping of oscillations in levitated droplets is significantly enhanced (Kremer, Kilzer & Petermann 2018), supporting the strong positive correlation between $E_{dis,bulk}$ and *Oh*. Therefore, all three types of viscous dissipation coexist for the impact of macroscale droplets.

At the nanoscale, a consensus has emerged in recent studies acknowledging that velocity gradients are notably intense throughout entire nanodroplets, and that the viscous dissipation caused by spreading rims is relatively insignificant (Li et al. 2015, 2017). Given the minimal scale of nanodroplets, some studies posited that impacting nanodroplets entirely fall in the boundary layer during impact (Li *et al*. 2017; Wang *et al*. 2020a), suggesting that boundary-layer dissipation is the primary mechanism (Li *et al*. 2017; Wang *et al*. 2020a). However, this viewpoint is worth discussing. The dominant velocity gradient within the boundary layer is typically dV_r/dz. Contrary to this, velocity contours from Li *et al*. (2015) and Wang *et al*. (2019) indicate that gradients dV_r/dr and dV_z/dz are violent throughout nanodroplets, contradicting the expected velocity characteristics of the boundary layer. Secondly, as the droplet scale decreases, the slip effect continuously enhances, diminishing the strength of boundary-layer dissipation. The slip effect has been observed at the microscale, as illustrated in figure 3(*a–d*), and it is more pronounced at the nanoscale, as figure 3(*f*) shows, suggesting a further weak influence of boundary-layer dissipation. Therefore, it is improbable that the boundary layer alone governs viscous dissipation at the nanoscale. The observed velocity gradients dV_r/dr and dV_z/dz align more closely with deformation-induced gradients in the bulk droplet, indicating that deformation-induced dissipation might be the predominant mechanism at the nanoscale. This occurrence can be attributed to the naturally high *Oh* at the nanoscale. Moreover, although previous studies have not focused on viscous dissipation due to rims at the nanoscale, Wang *et al*. (2023) showed that the rims do form during nanoscale impacts, particularly at high *We*. The formation of these rims likely results in a sharp reduction in radial velocity (V_r) at the entrance of rims, generating $E_{dis,rim}$. For the boundary-layer dissipation, although the slip effect is strongly enhanced and almost no boundary-layer gradients are present in velocity contours at the nanoscale, indicating an almost negligible intensity of $E_{dis,boundary}$ compared with other dissipation, it still exists owing to the presence of the solid walls. Therefore, the three types of viscous dissipation ($E_{dis,boundary}$, $E_{dis,rim}$ and $E_{dis,bulk}$) also contribute to the impact at the nanoscale as well.

According to the above discussion, a comprehensive understanding of the viscous dissipation mechanisms across different scales can be articulated. The decreased scale of droplets would increase *Oh*, highlighting the significance of $E_{dis,bulk}$ at both the nanoscale and microscale. Moreover, $E_{dis,bulk}$ would also become increasingly important as the viscosity of liquid increases. Therefore, to accommodate a broad range of *Oh*, $E_{dis,bulk}$ must be considered throughout the whole scale. Additionally, the presence of walls, which generate shear flow, ensures that boundary-layer dissipation ($E_{dis,boundary}$) occurs at all scales. The critical difference is that the slip effect becomes progressively more pronounced as the droplet scale decreases, so the strength of $E_{dis,boundary}$ continuously weakens. Lastly, spreading rims are a consistent observation in impacts across all scales when *We* is sufficiently high, approximately 30, as Wildeman *et al*. (2016) noted. Thus, the rim geometric head loss, $E_{dis,rim}$, also plays a crucial role throughout the scale.

3.3. *Modelling the maximum spreading factor throughout the whole scale*

Revealing the viscous dissipation mechanism is crucial for comprehending the impact dynamics of droplets; however, directly testing it is exceptionally intractable. The

maximum spreading factor serves as an extensively concerned feature parameter, and modelling this factor requires a profound understanding of viscous dissipation mechanism, making it a valuable bridge for inspecting this mechanism within the scientific community focused on droplet impact. This section will establish a model of β_{max} to thoroughly check the full-scale viscous dissipation mechanism thoroughly. Moreover, this model is also expected to predict a full spectrum of β_{max}, covering droplet scales from the macroscale to the nanoscale.

The model of β_{max} is established using the energy conservation equation, i.e. (1.1). Based on the spherical shape of a droplet before impacts, $E_{k,0}$ and $E_{s,0}$ can be expressed as

$$E_{k,0} = \tfrac{1}{12}\pi\rho D_0^3 V_0^2, \tag{3.1}$$

$$E_{s,0} = \gamma\pi D_0^2. \tag{3.2}$$

Assuming the cylindrical shape of the droplet at the maximum spreading state (Ukiwe & Kwok 2005), the surface energy at this state could be obtained as

$$E_{s,m} = \pi D_0^2 \gamma \left[\frac{1}{4}\beta_{max}^2 (1 - \cos\theta) + \frac{2}{3\beta_{max}} \right], \tag{3.3}$$

where the first term, $\pi D_0^2\gamma\beta_{max}^2(1 - \cos\theta)/4$, represents the surface energy of the upper and lower surfaces of spreading films, and the second term, $2\pi D_0^2\gamma/(3\beta_{max})$, stands for the surface energy of the periphery surface of spreading films. These terms are named $E_{s,m1}$ and $E_{s,m2}$, respectively, for discussion later.

The viscous dissipation during spreading is contributed by three terms, i.e. $E_{dis,boundary}$, $E_{dis,bulk}$ and $E_{dis,rim}$. As a result, the viscous dissipation during spreading can be expressed as

$$E_{dis} = E_{dis,boundary} + E_{dis,bulk} + E_{dis,rim}. \tag{3.4}$$

The expressions of $E_{dis,boundary}$ and $E_{dis,bulk}$ can be obtained by the integration of the dissipation functions of the shear flow (ϕ_s) and the extensional flow (ϕ_e), respectively, expressed as

$$E_{dis,boundary} = \int_0^{t_{sp}} \int_{\Omega_{boundary}} \phi_s \, d\Omega \, dt, \tag{3.5}$$

$$E_{dis,bulk} = \int_0^{t_{sp}} \int_{\Omega_{bulk}} \phi_e \, d\Omega \, dt, \tag{3.6}$$

where Ω_{bulk} is the volume occupied by the extensional flow, which approximates the volume of an entire droplet, and $\Omega_{boundary} \sim D_{max}^2\delta$ is the volume of the boundary layer. The general dissipation function is

$$\phi = \mu \left(\frac{\partial v_i}{\partial x_j} + \frac{\partial v_j}{\partial x_i} \right) \frac{\partial v_i}{\partial x_j}. \tag{3.7}$$

Considering $V_\theta = 0$, (3.7) can be simplified to

$$\phi = 2\mu \left[\left(\frac{\partial V_r}{\partial r} \right)^2 + \left(\frac{V_r}{r} \right)^2 + \left(\frac{\partial V_z}{\partial z} \right)^2 + \frac{1}{2}\left(\frac{\partial V_r}{\partial z} + \frac{\partial V_z}{\partial r} \right)^2 \right]. \tag{3.8}$$

At the macroscale, the no-slip condition holds so that ϕ_s can be simplified to $\sim\mu(V_0/\delta)^2$, as recognised by previous studies (Pasandideh-Fard *et al.* 1996; Ukiwe & Kwok 2005;

Wildeman *et al.* 2016). However, when the droplet diameter decreases from the macroscale to the nanoscale, the slip effect takes place and is continuously enhanced. To obtain the whole-scale expression of $E_{dis,boundary}$, according to figure 3(*d*), the slip effect is incorporated to revise the ϕ_s to

$$\phi_s \sim \mu \left(\frac{V_0}{\delta + \lambda} \right)^2 = \left(\frac{1}{1 + \dfrac{\lambda}{\delta}} \right)^2 \times \mu \left(\frac{V_0}{\delta} \right)^2 = C_{slip} \mu \left(\frac{V_0}{\delta} \right)^2, \quad (3.9)$$

where λ is the average slip length, and C_{slip} is the slip factor to describe the slip effect with its value ranging from 0 ($\lambda \to \infty$, free-slip) to 1 ($\lambda = 0$, no-slip). Integrating (3.5), the expression of boundary-layer dissipation is

$$E_{dis,boundary} \sim C_{slip} \mu \left(\frac{V_0}{\delta} \right)^2 (\beta_{max}^2 D_0^2 \delta) t_{sp}. \quad (3.10)$$

According to Wildeman *et al.* (2016), $t_{sp} = (D_0/V_0)(\beta_{max} - 1)$. This expression has been validated by impacts on both free-slip and no-slip surfaces, so it is expected to be universal throughout the scale. The thickness of the boundary layer is estimated by $\delta/D_0 \sim [t_{sp}/(Re\, D_0/V_0)]^{1/2}$ (Eggers *et al.* 2010; Wildeman *et al.* 2016). Substituting them in (3.10), the whole-scale expression of $E_{dis,boundary}$ is obtained as

$$E_{dis,boundary} = 0.6 C_{slip} \frac{\beta_{max}^2 (\beta_{max} - 1)^{1/2}}{Re^{1/2}} E_{k,0}, \quad (3.11)$$

where the prefactor of 0.6 is determined by Wildeman *et al.* (2016) by data at the macroscale.

The velocity distribution in the bulk droplet meets the extensional flow, expressed as (Wang *et al.* 2020*b*, 2024)

$$\left. \begin{array}{l} V_r = \dfrac{r}{R} V_{bulk}, \\[2mm] V_z = -\dfrac{2z}{R} V_{bulk}, \end{array} \right\} \quad (3.12)$$

where V_{bulk} is an equivalent velocity characterising the strength of extensional flow. Substituting (3.12) in (3.8), the dissipation function for the extensional flow is obtained as

$$\phi_e = 48\mu \frac{V_{bulk}^2}{\beta^2 D_0^2}. \quad (3.13)$$

Subsequently, substituting (3.13) in (3.6) and integrating (3.6) with respect to space, the bulk dissipation is transformed into

$$E_{dis,bulk} = 8\pi\mu D_0 V_{bulk}^2 \int_0^{t_{sp}} \frac{1}{\beta^2(t)} \, dt. \quad (3.14)$$

To ensure consistent estimations of $E_{dis,boundary}$ and $E_{dis,bulk}$, t_{sp} for calculating $E_{dis,bulk}$ is also $t_{sp} = (\beta_{max} - 1)D_0/V_0$. Here, the integration of time can be replaced by the integration of spreading factor, i.e. $dt = (D_0/V_0) \, d\beta$, expressed as

$$E_{dis,bulk} = 8\pi\mu D_0^2 C_{bulk}^2 V_0 \int_1^{\beta_{max}} \frac{1}{\beta^2} \, d\beta = 8\pi\mu D_0^2 C_{bulk}^2 V_0 \left(1 - \frac{1}{\beta_{max}} \right), \quad (3.15)$$

where $C_{bulk} = V_{bulk}/V_0$.

For the rim dissipation, Wildeman *et al.* (2016) found that it almost always consumes half of the initial kinetic energy when $We > 30$, expressed as

$$E_{dis,rim} = 0.5E_{k,0}. \tag{3.16}$$

This expression has been verified for impacting droplets on both free-slip and no-slip surfaces, so it is expected to be valid throughout the whole scale.

Substituting (3.1)–(3.3), (3.11), (3.15) and (3.16) in (1.1) and normalised by the initial surface energy, the model of β_{max} is finally obtained, expressed as

$$\frac{1}{12}We + 1 = \left[\frac{1}{4}\beta_{max}^2(1 - \cos\theta) + \frac{2}{3\beta_{max}}\right] + \frac{1}{20}C_{slip}We^{3/4}Oh^{1/2}\beta_{max}^2(\beta_{max} - 1)^{1/2}$$

$$+ 8C_{bulk}^2 We^{1/2}Oh\left(1 - \frac{1}{\beta_{max}}\right) + \frac{1}{24}We. \tag{3.17}$$

On the left-hand side of this equation, the first and second terms stand for the initial kinetic energy and initial surface energy, respectively; on the right-hand side, the four terms represent the surface energy at the maximum spreading state, boundary-layer dissipation, bulk dissipation and rim dissipation, respectively.

Here, an analysis is presented to demonstrate how the proposed model can effectively predict the dynamics of impacting droplets across various scales, taking water, a representative low-viscosity liquid, as an example. Water droplets exhibit an extremely low Ohnesorge number at the macroscale, approximately $O(10^{-3})$. Consequently, $E_{dis,bulk}$, which is proportional to Oh, becomes negligible compared with $E_{dis,boundary}$, which is proportional to $Oh^{1/2}$. However, as droplet diameter decreases, reaching the microscale or the nanoscale, the value of Oh for water droplets approaches $O(1)$. This shift results in the values of Oh and $Oh^{1/2}$ becoming comparable, making $E_{dis,bulk}$ and $E_{dis,boundary}$ similarly significant. This observation elucidates why, as the diameter of low-viscosity droplets reduces from the macroscale to the nanoscale, viscous dissipation becomes increasingly essential, extending from the boundary layer to the entire droplet. Furthermore, this model accounts for the change in boundary-layer dissipation across scales. As droplet diameters decrease from the macroscale to the nanoscale, C_{slip} decreases due to increased slip length. This change leads to a spontaneous reduction in boundary-layer dissipation. This trend is observable in figure 2, where β_{max} increases with decreasing scale when We, Oh and θ are held constant. Thus, the model provides a comprehensive perspective on how the dynamics of impacting droplets evolves with scales.

The proposed model has two independent parameters, C_{bulk} and C_{slip}, which govern the strength of $E_{dis,bulk}$ and $E_{dis,boundary}$, respectively. Given their independence, these parameters cannot be determined simultaneously by data fitting. Here, C_{bulk}, associated with the dissipation caused by droplet deformation, is expected to remain constant across all scales. Conversely, C_{slip} is influenced by the slip effect and thus varies depending on the scale of droplets. Specifically, C_{slip} approaches zero at the nanoscale and equals one at the macroscale. To determine these parameters, C_{bulk} should be first established by fitting data from either the nanoscale ($C_{slip} = 0$) or macroscale ($C_{slip} = 1$). Once C_{bulk} is determined, C_{slip} can be treated as an independent parameter.

This study has collected 16 series of data, including a diverse range of scales: five series at the macroscale from experiments (Series 1–5) (Stow & Hadfield 1981; Clanet *et al.* 2004; Antonini, Amirfazli & Marengo 2012; Abolghasemibizaki *et al.* 2019; Du, Zhang & Min 2021*b*); seven series at the microscale from our MDPD simulations (Series 6–12); and four series at the nanoscale from MD simulations (Series 13–16) (Wang *et al.* 2020*a*;
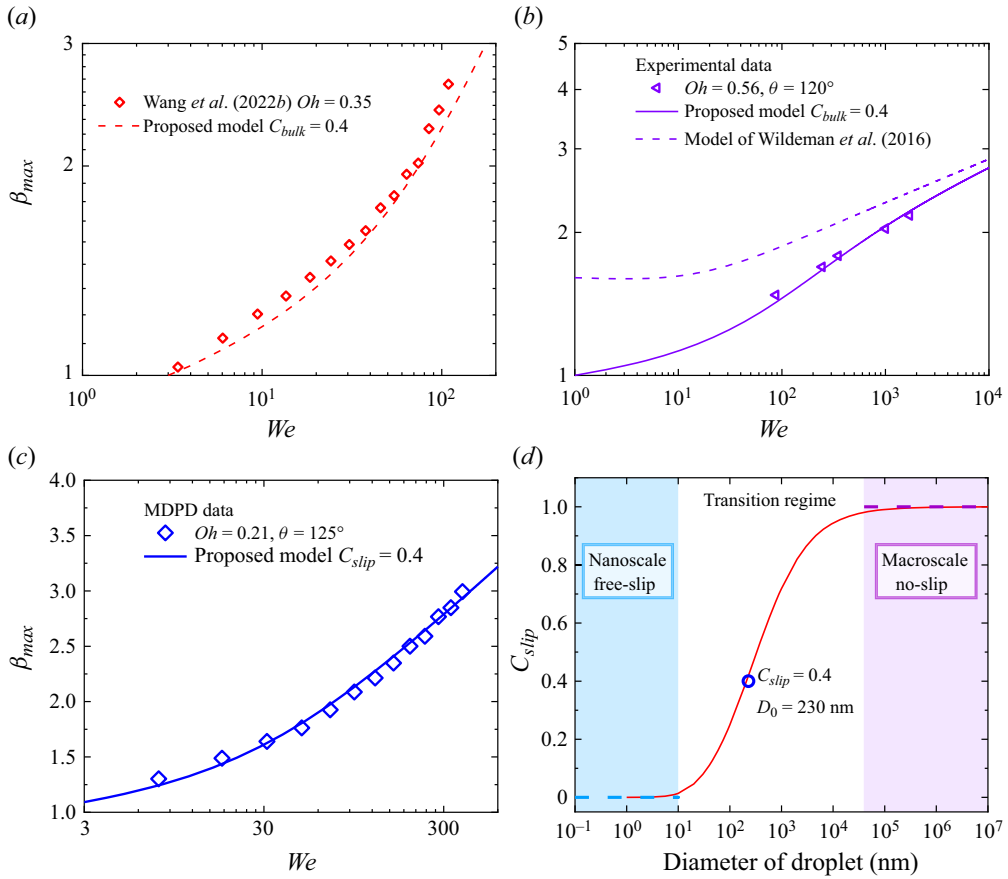
(*a*)

(*b*)

(*c*)

(*d*)

Figure 4. (*a*,*b*) Fitting C_{bulk} by the data of impacting nanodroplets with $Oh = 0.35$ on superhydrophobic surfaces with $\theta = 148°$ (Wang *et al.* 2022*b*) and of impacting macroscale droplets with $Oh = 0.56$ on superhydrophobic surfaces with $\theta = 120°$ (Du, Zhang & Min 2021*b*). (*c*) Fitting C_{slip} by the data of impacting microscale droplets with $Oh = 0.21$ on hydrophobic surfaces with $\theta = 125°$. (*d*) The relationship between C_{slip} and D_0 for water at $We = 300$ and $\theta = 125°$.

2022*b*; Zhang *et al.* 2014). Detailed information about these data series (Series 1–16) is available in supplementary material (table S2). In parameter determination, only one series of data from each scale is utilised to obtain C_{bulk} and C_{slip}. In contrast, the remaining data series are employed to validate the robustness and applicability of the proposed model.

Based on the above analysis, one series of nanoscale data (Series 14) is first employed to determine C_{bulk} by setting C_{slip} to 0. Subsequently, one series of macroscale data (Series 4) is used to validate the universality of the obtained C_{bulk}, fixing C_{slip} at 1. As figure 4(*a*) illustrates, with $C_{bulk} = 0.4$ and $C_{slip} = 0$, the proposed model successfully predicts β_{max} at the nanoscale. To convince us that $C_{bulk} = 0.4$ reasonably describes the velocity fields of impacting droplets, the velocity fields captured by simulations for the cases at $We = 30.6$, 45.7 and 73.9 in data Series 14 are used to validate it directly. Satisfactory agreement between the fitted C_{bulk} and the values of C_{bulk} by measuring the velocity fields is found (see supplementary material for details), directly proving this fitted result, $C_{bulk} = 0.4$. It is important to note that the significance of $E_{dis,bulk}$ is only pronounced for high Oh at the macroscale. Therefore, for the macroscale validation, β_{max} data of high-viscosity droplets (Series 4) from Du *et al.* (2021*b*) are chosen. As depicted in figure 4(*b*), the proposed

model, with $C_{bulk} = 0.4$ and $C_{slip} = 1$, also aligns satisfactorily with the β_{max} data at the macroscale. This occurrence effectively demonstrates that C_{bulk} remains constant across the scales. Furthermore, the model proposed by Wildeman *et al.* (2016) is also included for comparison in figure 4(*b*). For droplets with high *Oh* at the macroscale, our model, which accounts for deformation-induced bulk dissipation, exhibits significantly improved accuracy. This comparison preliminarily validates the effectiveness and accuracy of our proposed model in capturing the dynamics of droplet impacts across various scales.

Since C_{slip} varies with droplet scale, it cannot be straightforwardly determined through simple data fitting. In addition to the traditional dimensionless group (*We*, *Re* and θ) dominating the impact dynamics, the slip length also becomes a key parameter when considering dynamics across scales, which can be non-dimensionalised by D_0. Therefore, C_{slip} should be $C_{slip} = f_{slip}(We, Re, \lambda/D_0, \theta)$. Considering the estimation of $\delta \sim D_0[(\beta_{max} - 1)/(Re)]^{1/2}$ previously used in the derivation of (3.11), the key ratio, λ/δ, can be expressed as

$$\frac{\lambda}{\delta} \sim \frac{\lambda \, Re^{1/2}}{D_0(\beta_{max} - 1)^{1/2}}. \tag{3.18}$$

Incorporating this scaling relationship into $C_{slip} = (1 + \lambda/\delta)^{-2}$, with a dimensionless prefactor *c*, yields C_{slip} as

$$C_{slip} = \left(1 + \frac{c\lambda \, Re^{1/2}}{D_0(\beta_{max} - 1)^{1/2}}\right)^{-2}. \tag{3.19}$$

The parameters, *Re* and λ/D_0, are explicitly considered; while the dependence of *We* and θ is implicitly included in β_{max}. Here, λ is a material property, depending on the liquid involved and the substrate. In MDPD simulations, the liquid is fixed and only the contact angle is altered for the substrate. According to McBride & Law (2009), λ is not sensitive to the wettability of molecularly smooth hydrophobic surfaces. Therefore, $\lambda = 4.6$ nm measured from MDPD simulations, as shown in figure 3(*d*), is available for all MDPD cases in this study. When other liquids are considered or the property of substrates changes significantly, λ should be remeasured to obtain the correct one corresponding to the impact condition.

The dimensionless prefactor, *c*, is determined by fitting MDPD data. As shown in figure 4(*c*), for MDPD data of 230 nm water droplets (Series 8), fixing $\lambda = 4.6$ nm and using $c = 4$, the proposed model can align well with the data. Figure 4(*d*) shows the relationship between C_{slip} and D_0 at fixed $We = 300$, $\theta = 125°$ and $\lambda = 4.6$ nm for water. It is worth restating that the current literature has shown that $C_{slip} = 0$ for $D_0 < 10$ nm (Li *et al.* 2015; Wang *et al.* 2020*b*; Xie *et al.* 2020) and $C_{slip} = 1$ for $D_0 > 40$ µm (Wildeman *et al.* 2016). The predicted relationship of C_{slip} intriguingly approaches zero at the nanoscale and one at the macroscale, preliminarily validating the expression of C_{slip}.

3.4. *Validation of the β_{max} model*

In this section, the established model of β_{max} will be validated by data from the macroscale (Series 1–3 and 5), microscale (Series 6, 7 and 9–12) and nanoscale (Series 13, 15 and 16). For microscale data, C_{slip} is calculated by $\lambda = 4.6$ nm as mentioned above. Nonetheless, the lack of λ for macroscale and nanoscale data is an obstacle to validating the model. Fortunately, the orders of magnitude for D_0 are $O(1 \text{ mm})$ at the macroscale and $O(10 \text{ nm})$ at the nanoscale; therefore, $C_{slip} = 1$ and $C_{slip} = 0$ are reasonably used for respective scale data according to the literature (Li *et al.* 2015; Wildeman *et al.* 2016;
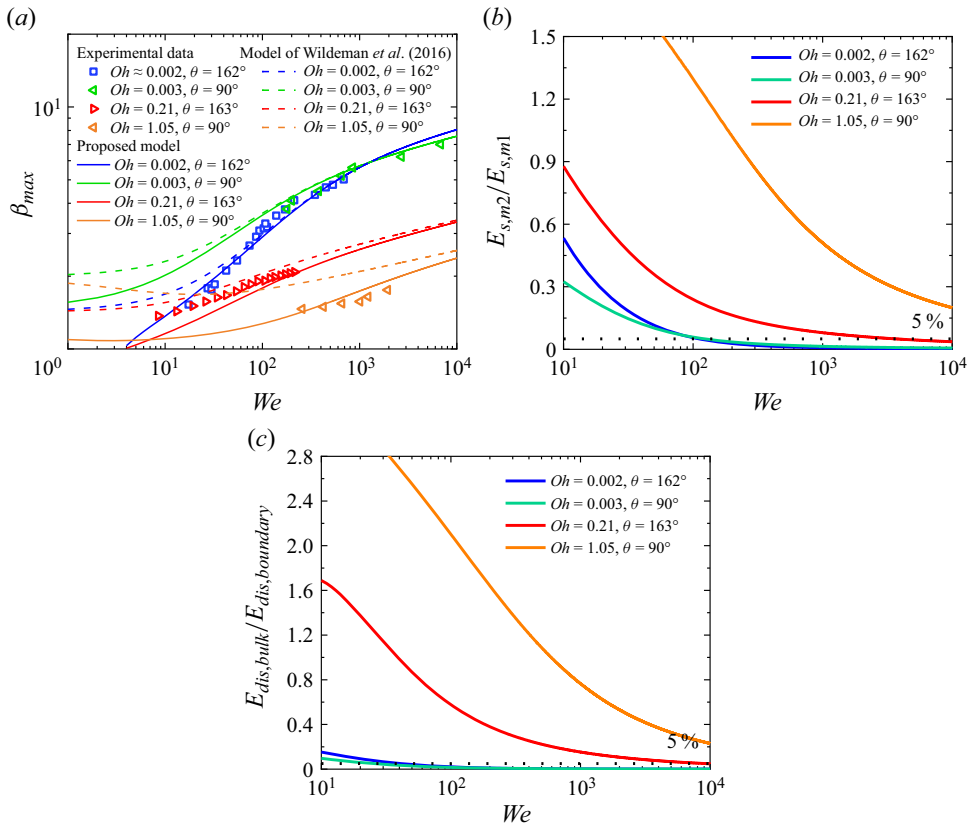
Figure 5. (*a*) Validating the proposed model and the model of Wildeman *et al*. (2016) by macroscale data of β_{max} in wide ranges of *We* from 8 to 6815, *Oh* from 0.002 to 1.05 and θ from 90° to 163°. The data are marked by blue (Antonini, Amirfazli & Marengo 2012), green (Stow & Hadfield 1981), red (Abolghasemibizaki *et al*. 2019) and orange (Clanet *et al*. 2004) points, respectively. (*b*) The proportion of the surface energy of the periphery surface ($E_{s,m2}$) to the one of the upper and lower surfaces ($E_{s,m1}$) and (*c*) the proportion of the bulk dissipation ($E_{dis,bulk}$) to the boundary-layer one ($E_{dis,boundary}$).

Wang *et al*. 2020*b*; Xie *et al*. 2020). In addition, the widely recognised model of β_{max} (Wildeman *et al*. 2016) that considers two kinds of viscous dissipation ($E_{dis,boundary}$ and $E_{dis,rim}$) has been examined at the macroscale and is also tested by these series of data to present how the added or modified energy terms in the proposed model affect the prediction results.

Here, the two models are tested first by four series of data at the macroscale, as shown in figure 5(*a*), with Series 1, millimetre-sized water droplets ($Oh = 0.002$) impacting superhydrophobic surfaces (Antonini *et al*. 2012); Series 2, millimetre-sized water droplets ($Oh = 0.003$) impacting weakly hydrophobic surfaces (Stow & Hadfield 1981); Series 3, millimetre-sized glycerol−water droplets ($Oh = 0.21$) impacting superhydrophobic surfaces (Abolghasemibizaki *et al.* 2019); Series 5, millimetre-sized silicone oil droplets ($Oh = 1.05$) (Clanet *et al*. 2004) impacting weakly hydrophobic surfaces. Based on these data series, extensive parametric ranges are covered, i.e. $8 \leq We \leq 6815$, $0.002 \leq Oh \leq 1.05$, $90° \leq \theta \leq 163°$.

For low-viscosity droplets (Series 1–2), both the proposed model and the model by Wildeman *et al*. (2016) demonstrate equally high prediction accuracy when *We* exceeds

100. This similarity in accuracy is attributed to the fact that the added energy terms in the current model ($E_{dis,bulk}$ and $E_{s,m2}$) are relatively insignificant compared with the existing terms ($E_{dis,boundary}$ and $E_{s,m1}$). This inference is supported by the energy proportions ($E_{dis,bulk}/E_{dis,boundary}$ and $E_{s,m2}/E_{s,m1}$) extracted from the present model, as depicted in figure 5(*b*,*c*). However, as *We* drops below 100, the dynamics accordingly changes: the spreading film at the maximum spreading state becomes thicker, and the maximum spreading factor (β_{max}) is reduced. Consequently, $E_{s,m2}$ becomes a non-negligible factor compared with $E_{s,m1}$. In this lower *We* range, the present model, which includes $E_{s,m2}$, delivers a more accurate prediction of β_{max} than the model of Wildeman *et al.* (2016). This enhanced accuracy in lower *We* scenarios underscores the importance of incorporating comprehensive energy terms to fully capture the dynamics of droplet spreading.

For high-viscosity droplets (Series 3), both the present model and the model by Wildeman *et al.* (2016) struggle to align with the data when *We* < 30. The current model tends to underestimate β_{max} in this range, which can be attributed to the difficulty in forming spreading rims at these Weber numbers. This limitation is also evident in the model of Wildeman *et al.* (2016); however, their model tends to overestimate β_{max} because it does not consider $E_{dis,bulk}$ and $E_{dis,m2}$. As *We* exceeds 30, the present model, which considers all forms of viscous dissipation, aligns satisfactorily with the data in both Series 3 and 4. This comprehensive approach is particularly crucial for high-viscosity droplets at the macroscale, where the effect of $E_{dis,bulk}$ becomes significant. This aspect of viscous dissipation is not included in the model by Wildeman *et al.*, leading to their model showing a substantial overestimation of β_{max} in these scenarios. Therefore, including $E_{dis,bulk}$ in the present model provides a more accurate representation of the spreading dynamics for high-viscosity droplets.

At the microscale, six data series (Series 6, 7 and 9–12) are employed to evaluate both the present model and the model by Wildeman *et al.* (2016). The first five series encompass a wide range of *We* from 3 to 930 and θ from 86° to 174° for droplets with a diameter of $D_0 = 230$ nm. The last series covers *We* from 50 to 1000, with $\theta = 125°$ and $D_0 = 1.15$ μm. As depicted in figure 6(*a*,*b*), the model of Wildeman *et al.* (2016) fails to predict the results in the first five series. For *We* < 90, it overestimates β_{max} due to the non-negligible contribution of $E_{s,m2}$ compared with $E_{s,m1}$ in this low *We* range. More importantly, their model does not account for the increasing importance of $E_{dis,bulk}$ at the microscale, attributable to higher *Oh* due to reduced droplet scales. As *We* > 90, the model conversely underestimates β_{max}, indicating an overestimation of boundary-layer dissipation due to the slip effect as they fixed $C_{slip} = 1$. The present model, however, incorporates not only $E_{dis,bulk}$ and $E_{s,m2}$ but also across-scale boundary-layer dissipation. Figure 6(*a*,*b*) shows that the present model aligns satisfactorily with MDPD simulation results. Further analysis of $E_{dis,bulk}/E_{dis,boundary}$ and $E_{s,m2}/E_{s,m1}$ extracted from the present model, as shown in figure 6(*c*,*d*), reveals that at low *We*, $E_{s,m2}$ and $E_{dis,bulk}$ are more significant than $E_{s,m1}$ and $E_{dis,boundary}$. This observation supports the idea that the overestimation of the model of Wildeman *et al.* (2016) is the lack of these terms at low Weber numbers. At high Weber numbers, $E_{s,m2}$ and $E_{dis,bulk}$ become negligible, affirming the dominance of $E_{s,m1}$ and $E_{dis,boundary}$ and verifying the underestimation of β_{max} by the model Wildeman *et al.* (2016) due to overestimated no-slip boundary-layer dissipation. To further validate the proposed expression for C_{slip} and the present model, Series 12 with larger $D_0 = 1.15$ μm at $\theta = 125°$ is also included in the comparison, as shown in figure 6(*e*). As anticipated, the model shows satisfactory agreement with simulation data, underscoring the universality and reliability of the expression of C_{slip}.

Eventually, the two models are tested by three series of nanoscale data, with Series 13, mW nanodroplets ($Oh = 0.35$) impacting hydrophobic surfaces (Wang *et al.* 2020*a*,*b*);
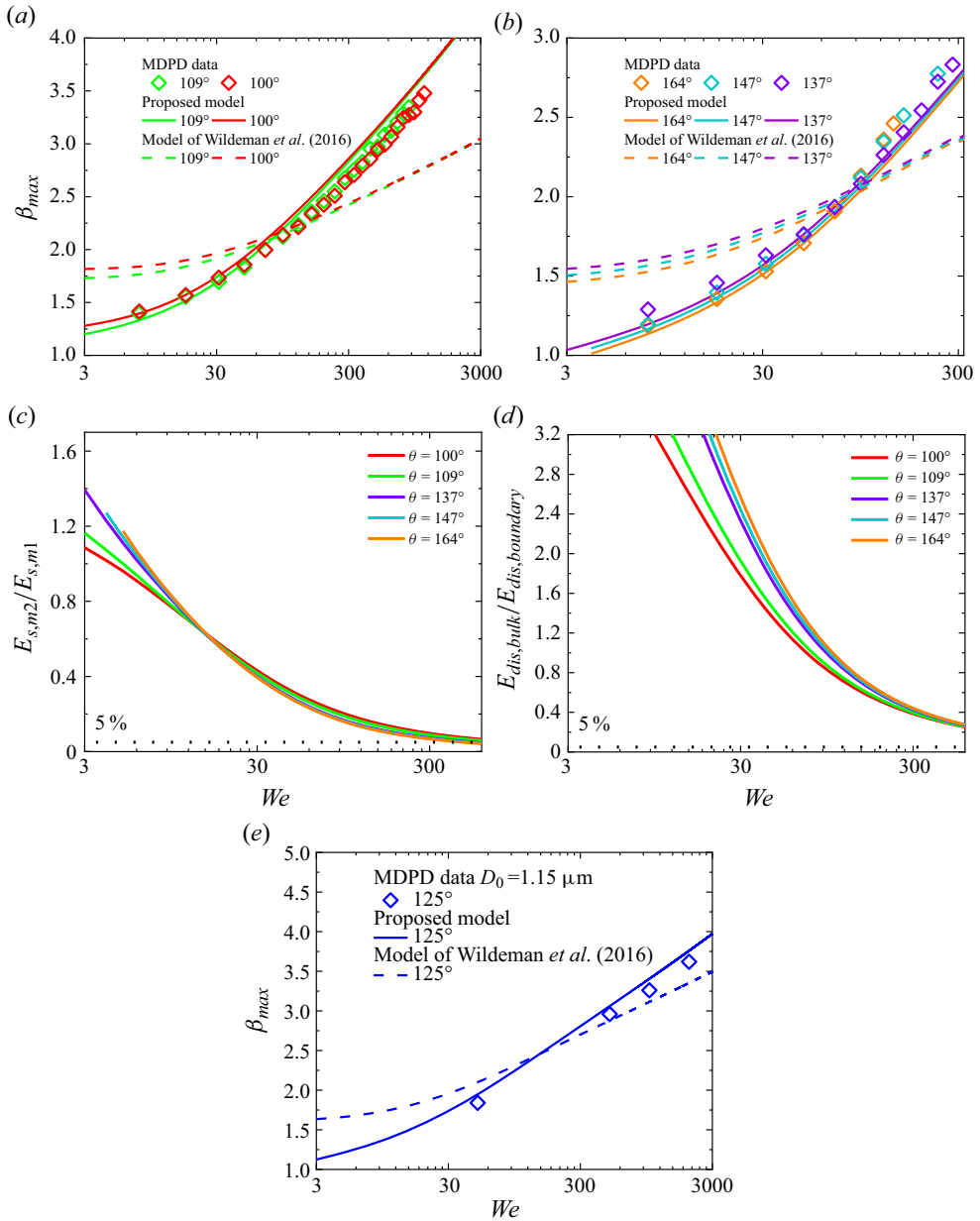
Figure 6. (*a*) Validating the proposed model and the model of Wildeman *et al.* (2016) by the MDPD data on (*a*) weak hydrophobic surfaces with θ from $100°$ to $109°$ and on (*b*) highly hydrophobic surfaces with θ from $138°$ to $174°$. (*c*) The proportion of the surface energy of the periphery surface ($E_{s,m2}$) to the one of the upper and lower surfaces ($E_{s,m1}$) and (*d*) the proportion of the bulk dissipation ($E_{dis,bulk}$) to the boundary-layer one ($E_{dis,boundary}$). (*e*) Validating the models by a larger water droplet with $D_0 = 1.15\ \mu m$ at $\theta = 125°$.

Series 15, mW nanodroplets ($Oh = 0.35$) impacting superhydrophobic surfaces; Series 16, Ar nanodroplets ($Oh = 0.48$) impacting superhydrophobic surfaces (Zhang *et al.* 2014). These data series span a wide range of *We*, *Oh* and θ. The enhanced slip effect at the nanoscale significantly reduces the boundary-layer viscous dissipation, rendering it almost
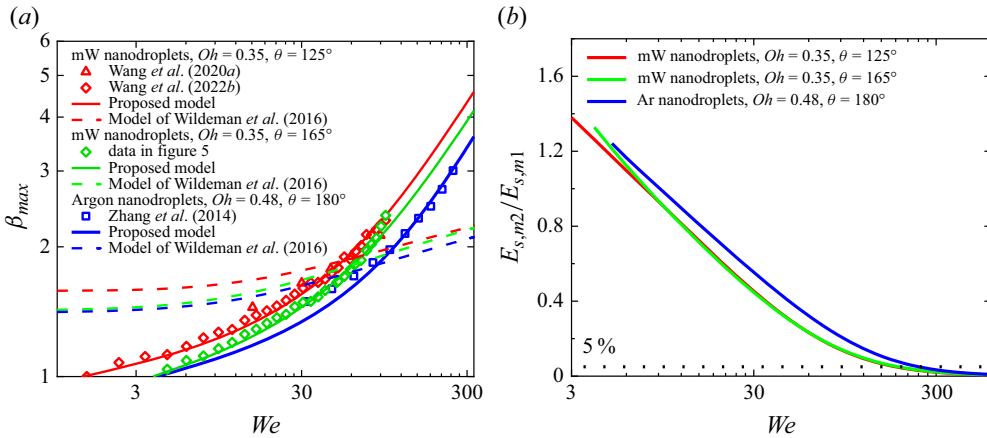
Figure 7. (*a*) Validating the proposed model and the model of Wildeman *et al*. (2016) by the data of β_{max} for impacting droplets at the nanoscale in wide ranges of *We*, *Oh* and θ from 1 to 290, from 0.35 to 0.48 and from 125° to 180°, respectively (Wang *et al*. 2020*a*, 2022*b*; Zhang *et al*. 2014). (*b*) The proportion of the surface energy of the periphery surface ($E_{s,m2}$) to the one of the upper and lower surfaces ($E_{s,m1}$).

negligible. Additionally, the increased *Oh* at this scale makes $E_{dis,bulk}$ more significant. Similar to observations at the microscale, the model Wildeman *et al*. (2016) tends to overestimate β_{max} in the low *We* range but underestimates it in the high *We* range, as shown in figure 7(*a*). In contrast, the proposed model effectively accounts for these changes, accurately capturing the boundary-layer viscous dissipation at the nanoscale. As shown in figure 7(*a*), the proposed model successfully predicts the data across these nanoscale series. In addition, the energy proportion $E_{s,m2}/E_{s,m1}$ is extracted from the proposed model (figure 7*b*). This ratio reinforces the reasoning behind the inaccuracy of the model of Wildeman *et al*. (2016) to predict β_{max} at the nanoscale, emphasising the importance of incorporating $E_{dis,bulk}$ and including slip effect for $E_{dis,boundary}$ to achieve accurate predictions in droplet impact dynamics.

4. Caveats and future directions

This section comments on the three forms of viscous dissipation, including $E_{dis,bulk}$, $E_{dis,boundary}$ and $E_{dis,rim}$, for an impacting droplet at different scales. The current analysis confirms that $E_{dis,bulk}$ dominates across the scales, as supported by the extensive testing previously discussed. Similarly, $E_{dis,boundary}$ is also essential throughout the whole scale. Regarding $E_{dis,rim}$, proposed as $0.5E_{k,0}$ by Wildeman *et al*. (2016) and adopted in this study, it is only effective when *We* exceeds 30. Below this threshold, spreading rims are difficult to form, eliminating the corresponding geometric head loss. This criterion for $E_{dis,rim}$ has been validated within the tested *Oh* range from 0.002 to 1.05. However, at a higher *Oh* of 1.54, no rim is observed even with *We* of 105, according to snapshots reported by Wang *et al*. (2019). Consequently, the proposed model significantly underestimates β_{max} over a wide *We* range from 15 to 105 when $E_{dis,rim}$ is included (figure 8). Removing $E_{dis,rim}$ from the model yields accurate predictions of β_{max} for droplets with extremely high *Oh*, proving the possible disappearance of $E_{dis,rim}$ in these conditions. Therefore, future research should also explore the criterion for $E_{dis,rim}$ about not only *We* but also *Oh*, especially for droplets with extremely large *Oh*.
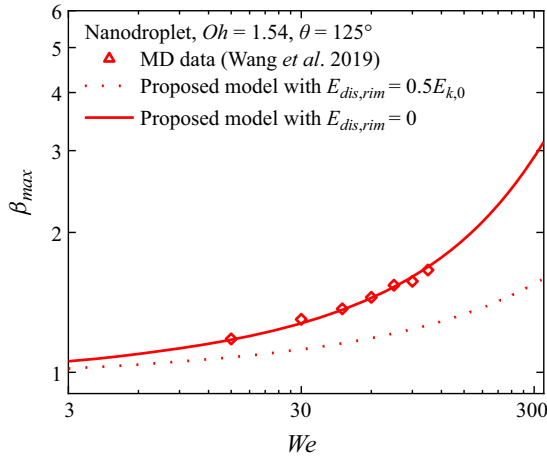
Figure 8. Validating the proposed model by the MD data of β_{max} by viscous impacting nanodroplets at $Oh = 1.54$ (Wang *et al.* 2019).

5. Conclusions

The impact dynamics of droplets at both the macroscale and the nanoscale have been extensively studied, revealing distinct behaviours at these extreme scales. Previous studies have attributed these differences to scale effects, suggesting that the droplet scale change dramatically alters the viscous dissipation mechanism. However, the underlying nature of how this mechanism evolves from the macroscale to the nanoscale has yet to be discovered. This study uses the MDPD simulation method to investigate impacting droplets on solid surfaces at the microscale. The aim is to bridge the gap between macroscale and nanoscale dynamics, shedding light on the continuous transition of the viscous dissipation mechanism across all scales.

From the velocity distribution extracted by MDPD simulations, three distinct forms of viscous dissipation are identified during spreading: bulk dissipation ($E_{dis,bulk}$) induced by droplet deformation; boundary-layer dissipation ($E_{dis,boundary}$) caused by shear flow near solid surfaces; rim dissipation ($E_{dis,rim}$) due to geometric head loss at the entrance of spreading rims. Subsequently, based on this insight, the viscous dissipation mechanisms at the macroscale and the nanoscale are revisited, and these three kinds of viscous dissipation are found to exist throughout the whole scale. Specifically, $E_{dis,bulk}$ is strongly influenced by Oh, with its significant increasing as decreasing droplet scale. The term $E_{dis,boundary}$ is sensitive to slip effects that become more pronounced with reducing scale, leading to a reduction in this form of dissipation. The term $E_{dis,rim}$ depends solely on rim formation and maintains consistent strength across scales, provided that spreading rims are formed.

Based on this comprehensive understanding of viscous dissipation mechanisms throughout scales, a β_{max} model that incorporates all these forms of dissipation is established. This model, validated with data spanning a wide range of *We*, *Oh* and θ, from the macroscale (millimetre-sized droplets), microscale ($D_0 = 230$ nm and 1.15 μm) and nanoscale (nanometre-sized droplets), demonstrates robust predictive power for β_{max}. Consequently, this work validates the full-scale viscous dissipation mechanism and provides a vital link in understanding the continuum of droplet impact behaviours from the macroscale to the nanoscale.

Supplementary material. Supplementary material is available at https://doi.org/10.1017/jfm.2024.911.

Declaration of interests. The authors report no conflict of interest.

Author ORCIDs.

Shao-Fei Zheng https://orcid.org/0000-0003-0539-8639;

Xiao-Dong Wang https://orcid.org/0000-0002-4533-6734.

REFERENCES

ABOLGHASEMIBIZAKI, M., DILMAGHANI, N., MOHAMMADI, R. & CASTANO, C.E. 2019 Viscous droplet impact on nonwettable textured surfaces. *Langmuir* **35**, 10752–10761.

ANTONINI, C., AMIRFAZLI, A. & MARENGO, M. 2012 Drop impact and wettability: from hydrophilic to superhydrophobic surfaces. *Phys. Fluids* **24**, 102104.

ATTANÉ, P., GIRARD, F. & MORIN, V. 2007 An energy balance approach of the dynamics of drop impact on a solid surface. *Phys. Fluids* **19**, 012101.

ARIENTI, M., PAN, W., LI, X. & KARNIADAKIS, G. 2011 Many-body dissipative particle dynamics simulation of liquid/vapor and liquid/solid interactions. *J. Chem. Phys.* **134**, 204114.

BERTOLA, V. 2009 An experimental study of bouncing Leidenfrost drops: comparison between Newtonian and viscoelastic liquids. *Intl J. Heat Mass Transfer* **52**, 1786–1793.

BORDBAR, A., TAASSOB, A., KHOJASTEH, D., MARENGO, M. & KAMALI, R. 2018 Maximum spreading and rebound of a droplet impacting onto a spherical surface at low weber numbers. *Langmuir* **34**, 5149–5158.

CHANDRA, S. & AVEDISIAN, C. 1991 On the collision of a droplet with a solid surface. *Proc. R. Soc.* A *Math. Phys. Engng Sci.* **432**, 13–41.

CHEN, H., NIE, Q. & FANG, H. 2020 Dynamic behavior of droplets on confined porous substrates: a many-body dissipative particle dynamics study. *Phys. Fluids* **32**, 102003.

CLANET, C., BÉGUIN, C., RICHARD, D. & QUÉRÉ, D. 2004 Maximal deformation of an impacting drop. *J. Fluid Mech.* **517**, 199–208.

DU, B., CHENG, Y., YANG, S., XU, W., LAN, Z., WEN, R. & MA, X. 2020 Preferential vapor nucleation on hierarchical tapered nanowire bunches. *Langmuir* **37**, 774–784.

DU, J., WANG, X., LI, Y., MIN, Q. & WU, X. 2021*a* Analytical consideration for the maximum spreading factor of liquid droplet impact on a smooth solid surface. *Langmuir* **37**, 7582–7590.

DU, J., ZHANG, Y. & MIN, Q. 2021*b* Numerical investigations of the spreading and retraction dynamics of viscous droplets impact on solid surfaces. *Colloids Surf.* A **609**, 125649.

EGGERS, J., FONTELOS, M.A., JOSSERAND, C. & ZALESKI, S. 2010 Drop dynamics after impact on a solid wall: theory and simulations. *Phys. Fluids* **22**, 062101.

GAD-EL-HAK, M. 1999 The fluid mechanics of microdevice – the Freeman scholar lecture. *J. Fluids Engng* **121**, 5–33.

GALLIKER, P., SCHNEIDER, J., EGHLIDI, H., KRESS, S., SANDOGHDAR, V. & POULIKAKOS, D. 2012 Direct printing of nanostructures by electrostatic autofocussing of ink nanodroplets. *Nat. Commun.* **3**, 890.

GHOUFI, A., MALFREYT, P. & TILDESLEY, D.J. 2016 Computer modelling of the surface tension of the gas–liquid and liquid–liquid interface. *Chem. Soc. Rev.* **45**, 1387–1409.

GLASSCOTT, M.W., PENDERGAST, A.D., GOINES, S., BISHOP, A.R., HOANG, A.T., RENAULT, C. & DICK, J.E. 2019 Electrosynthesis of high-entropy metallic glass nanoparticles for designer, multi-functional electrocatalysis. *Nat. Commun.* **10**, 2650.

GROOT, R.D. & WARREN, P.B. 1997 Dissipative particle dynamics: bridging the gap between atomistic and mesoscopic simulation. *J. Chem. Phys.* **107**, 4423–4435.

JAMALI, S., BOROMAND, A., KHANI, S., WAGNER, J., YAMANOI, M. & MAIA, J. 2015 Generalized mapping of multi-body dissipative particle dynamics onto fluid compressibility and the Flory-Huggins theory. *J. Chem. Phys.* **142**, 164902.

JOSSERAND, C. & THORODDSEN, S.T. 2016 Drop impact on a solid surface. *Annu. Rev. Fluid Mech.* **48**, 365–391.

KOBAYASHI, K., KONNO, K., YAGUCHI, H., FUJII, H., SANADA, T. & WATANABE, M. 2016 Early stage of nanodroplet impact on solid wall. *Phys. Fluids* **28**, 032002.

KOISHI, T., YASUOKA, K. & ZENG, X.C. 2017 Molecular dynamics simulation of water nanodroplet bounce back from flat and nanopillared surface. *Langmuir* **33**, 10184–10192.

KREMER, J., KILZER, A. & PETERMANN, M. 2018 Simultaneous measurement of surface tension and viscosity using freely decaying oscillations of acoustically levitated droplets. *Rev. Sci. Instrum.* **89**, 015109.

LAAN, N., DE BRUIN, K.G., BARTOLO, D., JOSSERAND, C. & BONN, D. 2014 Maximum diameter of impacting liquid droplets. *Phys. Rev. Appl.* **2**, 044018.

LEE, J.B., DEROME, D., DOLATABADI, A. & CARMELIET, J. 2016*a* Energy budget of liquid drop impact at maximum spreading: numerical simulations and experiments. *Langmuir* **32**, 1279–1288.

LEE, J.B., LAAN, N., DE BRUIN, K.G., SKANTZARIS, G., SHAHIDZADEH, N., DEROME, D., CARMELIET, J. & BONN, D. 2016*b* Universal rescaling of drop impact on smooth and rough surfaces. *J. Fluid Mech.* **786**, R4.

LI, B.X., LI, X.H. & CHEN, M. 2017 Spreading and breakup of nanodroplet impinging on surface. *Phys. Fluids* **29**, 012003.

LI, X.H., ZHANG, X.X. & CHEN, M. 2015 Estimation of viscous dissipation in nanodroplet impact and spreading. *Phys. Fluids* **27**, 052007.

LI, Z., BIAN, X., TANG, Y.H. & KARNIADAKIS, G.E. 2018 A dissipative particle dynamics method for arbitrarily complex geometries. *J. Comput. Phys.* **355**, 534–547.

LI, Z., HU, G.H., WANG, Z.L., MA, Y.B. & ZHOU, Z.W. 2013 Three dimensional flow structures in a moving droplet on substrate: a dissipative particle dynamics study. *Phys. Fluids* **25**, 072103.

LOTH, E. 2008 Compressibility and rarefaction effects on drag of a spherical particle. *AIAA J.* **46**, 2219–2228.

LOTH, E., TYLER DASPIT, J., JEONG, M., NAGATA, T. & NONOMURA, T. 2021 Supersonic and hypersonic drag coefficients for a sphere. *AIAA J.* **59**, 3261–3274.

MADEJSKI, J. 1976 Solidification of droplets on a cold surface. *Intl J. Heat Mass Transfer* **19**, 1009–1013.

MAO, T., KUHN, D.C. & TRAN, H. 1997 Spread and rebound of liquid droplets upon impact on flat surfaces. *AIChE J.* **43**, 2169–2179.

MCBRIDE, S.P. & LAW, B.M. 2009 Viscosity-dependent liquid slip at molecularly smooth hydrophobic surfaces. *Phys. Rev.* E **80**, 060601.

MURTOLA, T., BUNKER, A., VATTULAINEN, I., DESERNO, M. & KARTTUNEN, M. 2009 Multiscale modeling of emergent materials: biological and soft matter. *Phys. Chem. Chem. Phys.* **11**, 1869–1892.

NIE, Q.C., ZHONG, Y.H. & FANG, H.S. 2019 Study of a nanodroplet breakup through many-body dissipative particle dynamics. *Phys. Fluids* **31**, 042007.

PASANDIDEH-FARD, M., QIAO, Y.M., CHANDRA, S. & MOSTAGHIMI, J. 1996 Capillary effects during droplet impact on a solid surface. *Phys. Fluids* **8**, 650–659.

SRIVASTAVA, T. & KONDARAJU, S. 2020 Analytical model for predicting maximum spread of droplet impinging on solid surfaces. *Phys. Fluids* **32**, 092103.

STOW, C.D. & HADFIELD, M.G. 1981 An experimental investigation of fluid flow resulting from the impact of a water drop with an unyielding dry surface. *Proc. R. Soc.* A *Math. Phys. Engng Sci.* **373**, 419–441.

UKIWE, C. & KWOK, D.Y. 2005 On the maximum spreading diameter of impacting droplets on well-prepared solid surfaces. *Langmuir* **21**, 666–673.

VISSER, C.W., FROMMHOLD, P.E., WILDEMAN, S., METTIN, R., LOHSE, D. & SUN, C. 2015 Dynamics of high-speed micro-drop impact: numerical simulations and experiments at frame-to-frame times below 100 ns. *Soft Matt.* **11**, 1708–1722.

VISSER, C.W., TAGAWA, Y., SUN, C. & LOHSE, D. 2012 Microdroplet impact at very high velocity. *Soft Matt.* **8**, 10732–10737.

WANG, Y.-B., WANG, X.-D., YANG, Y.-R. & CHEN, M. 2019 The maximum spreading factor for polymer nanodroplets impacting a hydrophobic solid surface. *J. Phys. Chem.* C **123**, 12841–12850.

WANG, Y.-B., WANG, Y.-F., GAO, S.-R., YANG, Y.-R., WANG, X.-D. & CHEN, M. 2020*a* Universal model for the maximum spreading factor of impacting nanodroplets: from hydrophilic to hydrophobic surfaces. *Langmuir* **36**, 9306–9316.

WANG, Y.-B., WANG, Y.-F., WANG, X., ZHANG, B.-X., YANG, Y.-R., LEE, D.-J., WANG, X.-D. & CHEN, M. 2021*b* Splash of impacting nanodroplets on solid surfaces. *Phys. Rev. Fluids* **6**, 094201.

WANG, Y.-B., WANG, Y.-F., YANG, Y.-R., WANG, X.-D. & CHEN, M. 2021*a* Spreading time of impacting nanodroplets. *J. Phys. Chem.* B **125**, 5630–5635.

WANG, Y.-F., WANG, Y.-B., CAI, Z.-H., MA, Q., YANG, Y.-R., ZHENG, S.-F., LEE, D.-J. & WANG, X.D. 2024 Binary collision dynamics of equal-sized nanodroplets. *J. Fluid Mech.* **979**, A25.

WANG, Y.-F., WANG, Y.-B., HE, X., ZHANG, B.-X., YANG, Y.-R., WANG, X.-D. & LEE, D.-J. 2022*a* Retraction dynamics of low-viscosity nanodroplets: from hydrophobic to hydrophilic surfaces. *J. Mol. Liq.* **355**, 118963.

WANG, Y.-F., WANG, Y.-B., HE, X., ZHANG, B.-X., YANG, Y.-R., WANG, X.-D. & LEE, D.-J. 2022*b* Scaling laws of the maximum spreading factor for impact of nanodroplets on solid surfaces. *J. Fluid Mech.* **937**, A12.

WANG, Y.-F., WANG, Y.-B., XIE, F.-F., LIU, J.-Y., WANG, S.-L., YANG, Y.-R., GAO, S.-R. & WANG, X.-D. 2020*b* Spreading and retraction kinetics for impact of nanodroplets on hydrophobic surfaces. *Phys. Fluids* **32**, 092005.

WANG, Y.-F., WANG, Y.-B., ZHANG, C.-L., HE, X., YANG, Y.-R., ZHENG, S.-F., LEE, D.-J. & WANG, X.-D. 2023 Retraction and bouncing dynamics of nanodroplets upon impact on superhydrophobic surfaces. *Phys. Fluids* **35**, 032012.

WARREN, P.B. 2001 Hydrodynamic bubble coarsening in off-critical vapor-liquid phase separation. *Phys. Rev. Lett.* **87**, 225702.

WARREN, P.B. 2003 Vapor-liquid coexistence in many-body dissipative particle dynamics. *Phys. Rev. E* **68**, 066702.

WILDEMAN, S., VISSER, C.W., SUN, C. & LOHSE, D. 2016 On the spreading of impacting drops. *J. Fluid Mech.* **805**, 636–655.

WORTHINGTON, A.M. 1876 On the forms assumed by drops of liquids falling vertically on a horizontal plate. *Pro. R. Soc. Lond.* **25**, 261–271.

XIE, F.F., LV, S.H., YANG, Y.R. & WANG, X.D. 2020 Contact time of a bouncing nanodroplet. *J. Phys. Chem. Lett.* **11**, 2818–2823.

YAMADA, T., YUAN, J. & SUNDEN, B.A. 2015 Application of many-body dissipative particle dynamics to determine liquid characteristics. *Intl J. Numer. Meth. Heat Fluid Flow* **25**, 1619–1637.

YANG, J.C., QI, T.Y., HAN, T.Y., ZHANG, J. & NI, M.J. 2018 Elliptical spreading characteristics of a liquid metal droplet impact on a glass surface under a horizontal magnetic field. *Phys. Fluids* **30**, 012101.

YARIN, A.L. & WEISS, D.A. 1995 Impact of drops on solid surfaces: self-similar capillary waves, and splashing as a new type of kinematic discontinuity. *J. Fluid Mech.* **283**, 141–173.

ZARIN, N.A. 1970 Measurement of non-continuum and turbulence effects on subsonic sphere drag. NASA No. NASA-CR-1585.

ZHANG, R., FAROKHIRAD, S., LEE, T. & KOPLIK, J. 2014 Multiscale liquid drop impact on wettable and textured surfaces. *Phys. Fluids* **26**, 082003.

ZHAO, J., CHEN, S., ZHANG, K. & LIU, Y. 2021 A review of many-body dissipative particle dynamics (MDPD): theoretical models and its applications. *Phys. Fluids* **33**, 112002.